Journal of CO2 Utilization 97 (2025) 103106

Contents lists available at ScienceDirect

Journal of CO2 Utilization

journal homepage: www.elsevier.com/locate/jcou

Electrodeposited copper-cuprite layers modified with rGO for light-supported conversion of CO_2 to methane and ethylene

Krzysztof Mech [a,*], Patrycja Kolbusz [a], Andrzej Sławek [a], Mateusz Marzec [a], Edit Csapó [b,c]

[a] AGH University of Krakow, Academic Centre of Materials and Technology, al. Mickiewicza 30, Kraków 30-059, Poland
[b] MTA-SZTE Lendület "Momentum" Noble Metal Nanostructures Research Group, University of Szeged, Rerrich B. sqr. 1, Szeged H-6720, Hungary
[c] Interdisciplinary Excellence Center, Department of Physical Chemistry and Materials Science, University of Szeged, Rerrich B. sqr. 1, Szeged H-6720, Hungary

ARTICLE INFO

Keywords:
Electrodeposition
Composite coatings
CO_2 conversion
Photoelectrocatalysis

ABSTRACT

Cu-Cu_2O-rGO composite layers were electrodeposited for the first time from alkaline copper(II) lactate-based electrolytes containing dispersed rGO flakes. The properties of electrodeposited composite materials are strongly affected by applied potentials. Obtained layers were investigated towards their catalytic activity in electro- and photoelectrochemical artificial CO_2-based synthesis of hydrocarbons. The effect of applied potential on the morphology, crystallographic structure, band gap, and conduction and valence band location was investigated. The catalytic performance of the electrodeposited layers was analyzed in CO_2-saturated $KHCO_3$ electrolyte under the dark and at light illumination applying different conversion potentials. The stability of the obtained layers was analysed based on XPS and XAS results. Maximal Faradaic efficiencies for methane and ethylene formation were achieved in the presence of light and amounted to 10 and 9.91%, respectively. Reported results indicate that the presence of rGO in deposited layers significantly affects the band structure of electrodeposited layers. It was also observed that even slight modification of electrodeposition or conversion potential results in noticeable differences in Faradaic efficiency corresponding to hydrocarbons formation.

1. Introduction

Electrochemical (EC) and photoelectrochemical (PEC) conversion of carbon dioxide (CO_2) is important for many reasons related mainly to addressing environmental challenges and developing sustainable energy solutions [1–3]. Carbon dioxide mitigation is considered the primary driver for the development of materials for electrochemical and photoelectrochemical conversion of CO_2 due to the increasing impact of its emissions on climate change. Conversion of CO_2 into useful products, such as fuels or chemicals, is the perfect approach providing possibilities for the reduction of net emissions of greenhouse gases. That is why so much effort is paid to the utilization of CO_2 conversion in the production of carbon-neutral or carbon-negative fuels, like methane [4–6], ethylene [7,8], ethanol [9] or methanol [10,11], which can be used as energy carriers without contributing to additional carbon emissions [1]. CO_2 can be used also as a feedstock for the production of valuable chemicals. Electrochemical conversion processes can facilitate the synthesis of various chemicals, providing an alternative to traditional methods that often rely on fossil fuels as feedstocks [12,13].

EC and PEC are also considered a promising methods for renewable energy storage-oriented systems [14,15]. The electrochemical/photoelectrochemical conversion of CO_2 can be coupled with renewable energy sources such as solar or wind power. By using excess renewable energy to drive these conversion processes, it becomes possible to store intermittent renewable energy in the form of chemical fuels, providing a means for renewable energy storage [13,16].

Research in electrochemical and photoelectrochemical CO_2 conversion involves developing new materials, catalysts, and technologies [6,17–19]. These advancements not only contribute to addressing climate change but also drive technological innovation, potentially leading to the development of more efficient and sustainable energy technologies. All mentioned factors make EC and PEC conversion of CO_2 especially important due to its huge potential concerning mitigation of climate change, storing renewable energy, producing carbon-neutral fuels and chemicals, and contributing to global efforts towards a more sustainable and environmentally friendly future.

In recent years, many papers devoted to the engineering of materials that may be utilized in CO_2 conversion have been published. Yet, a

* Correspondence to: AGH University of Krakow, Academic Centre of Materials and Technology, Bldg. D-16, room 2.26, al. Mickiewicza 30, Krakow 30-059, Poland.
E-mail address: kmech@agh.edu.pl (K. Mech).

https://doi.org/10.1016/j.jcou.2025.103106
Received 7 February 2025; Received in revised form 16 April 2025; Accepted 6 May 2025
Available online 12 May 2025

considerable number of investigated materials exhibit drawbacks such as low efficiency, stability or selectivity [20]. To meet the criteria for commercial viability, catalysts for the CO_2 reduction reaction (CO_2RR) must attain a Faradaic efficiency (FE) exceeding 90 % for current densities surpassing 200 mA/cm^2. Additionally, these catalysts should demonstrate stability for a minimum of 1000 hours to be economically feasible [21]. Currently, existing catalysts fall below these benchmarks, underscoring the imperative for further investigations focused on creating new catalysts endowed with stability, selectivity, and efficiency. That is why , many different materials for potential application PE and PEC CO_2 conversion have been investigated [22,23]. One of the interesting, widely investigated materials are copper-based catalysts [24]. Copper due to its unique properties supporting the formation of double C=C bond is most often used for this purpose [25]. The coupling of copper with p-type Cu_2O creates possibilities for the utilization of light and thus limitation of energy consumption. Light is also considered a factor that strongly affects the kinetics and mechanism of electrode processes and thus selectivity of the catalytic materials. De Brito et al. conducted investigations into the photoelectrochemical conversion of CO_2 utilizing Cu/Cu_2O composites, with a primary focus on the impact of pH on the distribution of obtained products in the syngas [26]. Kas et al. demonstrated that Cu_2O, regardless of its structural properties, may effectively facilitate the formation of ethylene [27]. This finding was substantiated by Ren et al., who determined that the efficiency of the reduction of CO_2 to ethanol and ethylene at the Cu_2O surface is comparable to that observed for polycrystalline copper [28]. It was also observed by Kas et al. that the utilization of Cu_2O-based nanoparticles enables the adjustment of hydrocarbon production selectivity [27]. Shang et al. indicated possibilities of electrochemical reduction of CO_2 to ethylene with the use of core-shell copper/cuprous oxide structures [29]. Previously Mech et al. reported the EC and PEC performance of electrodeposited Cu-Cu_2O composite materials toward the conversion of CO_2 into hydrocarbons [30]. They observed that Faradaic efficiency, selectivity and overpotential related to maximal CH_4 and C_2H_4 production may be tuned by proper adjustment of electrodeposition potential. Their results indicated that the presence of light, even at the conversion potential window in which Cu_2O is considered unstable affects the kinetics and mechanism of electrode reactions resulting in the formation of several conversion products. Authors observed also that decrease in $E_{dep.}$ results in increased ethylene selectivity while the opposite effect was observed for methane. In the literature there are many reports showing that electrodeposition is method that through proper adjustment of process parameters provides possibilities for synthesis of pure metal [31,32], alloy [33,34], semiconducting [35,36], and multicomponent composite layers of controlled composition, morphology, and structure what is crucial in term of development of catalytic coatings [37–39]. All these factors in turn affect among other properties the final electrocatalytic or photoelectrocatalytic performance of obtained layers.

The tuning of the electrochemical performance may be also realized through the modification of catalysts/photocatalysts with carbon-derived materials such as graphene [9,40], graphene oxide (GO) [41] or reduced graphene oxide (rGO) [42]. Reduced graphene oxide is a graphene oxide derivative material. GO is synthesized by the oxidation and exfoliation of graphite. The reduction process involves the removal of functional groups containing oxygen from GO, resulting in a material with properties that are distinct from both graphene oxide and pristine graphene [43]. One of the most significant properties of rGO is its electrical conductivity. The reduction process restores the sp2 hybridization of carbon atoms, enhancing the electron mobility and allowing for efficient charge transport [44]. The reduction of GO can lead to the restoration of the graphene structure, contributing to a high specific surface area [45]. It is advantageous for applications related to energy storage devices, catalysis, and sensors, where a large surface area can enhance reactivity and adsorption.

Modification of photocatalytic properties with reduced graphene oxide (rGO) may be beneficial for several reasons, particularly in the context of improving the performance of photo- and photoelectrocatalysts. Shin et al. reported that rGO may successfully enhance charge separation reducing the electron-hole recombination effect in photocatalytic CO_2 reduction [46]. The positive effect of rGO on charge transfer limitation was also indicated by Tu et al. in photoelectrochemical 2,4 dichlorophenol degradation [47]. It was found that rGO significantly prevents trap-assisted and bimolecular charge carrier recombination and improves charge separation. This in turn results in increased charge carriers' lifetime and quantity of charge transported to catalytic active sites [48].

rGO can also expand the absorption spectral range of many metal oxides weakly absorbing light in the visible range [49,50]. The effect may be related to the highly porous rGO-based materials which in turn may result in multiple reflections of light inside the layers and thus improve the light absorption [51,52]. The coupling of rGO with semiconductors may also result in increased surface area which enhances the availability of active sites for adsorption and reaction, leading to improved catalytic performance [53].

A combination of Cu_2O and rGO in terms of light-supported CO_2 conversion was also proved to be beneficial. Liu et al. reported that rhombic dodecahedral Cu_2O/rGO composite exhibits high visible-light activity toward the reduction of CO_2 to methanol. It was reported that the effect may be related to increased adsorption of carbonate anions resulting from the presence of positively charged dodecahedral Cu_2O/rGO. The enhanced kinetics of methanol generation may be also explained by the participation of the rGO in the transport of photoexcited electrons from the Cu_2O valence band to the surface [54]. An et al. also reported the positive effect of the combination of Cu_2O and rGO in designing the catalytic materials for the photoelectrochemical reduction of CO_2. They reported extremely high efficiency of photoreduction of CO_2 to CO – the only product detected in syngas. The formation of rGO/Cu_2O heterojunction resulted in a 2-time increase of reduction kinetics and the photoreduction of CO_2 resulted in the formation of CO. The authors reported also that the presence of rGO resulted in a significant improvement in Cu_2O stability. The increased efficiency was attributed to the limitation of the charge recombination effect, enhanced charge transfer, and increased stability of Cu_2O resulting from the presence of rGO [55]. It shows that the incorporation of rGO into photocatalytic materials can significantly enhance their performance by improving charge carrier dynamics, limiting electron-hole recombination, and protecting Cu_2O against its photodegradation. Intensified effective charge transfer, a more developed surface area, and a higher number of reaction sites were also reported by Wang et as the main factor supporting photocatalytic CO_2 reduction [56]. The enhancement of Faradaic efficiency for conversion of CO_2 to CO resulting from the presence of rGO was also reported by Bisetto et al. for electrocatalytic process conducted at dark conditions [57]. Peng et al. reported that the coexistence of Cu^0-Cu^+ states and rGO promoted the activation of CO_2 molecules, enhanced C-C coupling and improved stability of Cu-Cu_2O/rGO composite materials. The effect is also related to the size effect of Cu-Cu_2O particles loaded onto rGO nanosheets. Synthesized Cu-Cu_2O/rGO materials favour mainly the formation of ethylene and much lower amounts of ethane and hydrogen [58]. Carminati et al. underlined that regardless of the positive and synergic effects of coupling rGO with semiconductors, the mechanisms supporting charge carrier dynamics are still not fully understood [49]. All the above-mentioned results are related to Cu_2O-rGO-based materials tested toward CO_2 reduction in electrochemical or photocatalytic processes. Herein were analysed catalytic activity, efficiency and selectivity of Cu-Cu_2O-rGO layers polarized at different overpotentials and also simultaneously irradiated with Xe lamp. Recently we published results showing the possibilities of utilization of Cu-Cu_2O composite films as catalytic layers allowing photoelectrochemical conversion of CO_2 to C_2H_4, CH_4, CO, and H_2 [30]. Moreover, we showed that irradiation of the catalytic layers resulted in modification of the kinetics of electrode

processes and thus Faradaic efficiencies related to the formation of particular gas products. In this study, we introduce reduced graphene oxide into the electrodeposition bath, which significantly alters both the physicochemical and electronic properties of the electrodeposited composite layers. This modification leads to pronounced changes in both band gap and flat band potentials. Moreover, herein we present a detailed analysis of the effect of rGO incorporation on energy band alignment versus redox potentials corresponding to CO_2 reduction reactions, offering mechanistic insights into the photoelectrochemical behaviour of the system. Compared to the previous study describing the effect of electrodeposition potential and conversion potential on photoelectrochemical performance, the current study extends catalytic performance by introducing the role of rGO in the modification of the properties crucial in terms of electrochemical and photoelectrochemical CO_2 conversion.

In present studies we described synthesis and characterization of Cu-Cu_2O-rGO composite catalytic layers designed for CO_2 conversion. The EC and PEC performance of materials was characterized in terms of selectivity and Faradaic efficiency. The composite layers were electrodeposited at varying potentials ($E_{dep.}$). It was observed that the value of applied $E_{dep.}$ exert a notable impact on phase composition, morphology, band gap (E_g), as well as on conduction, and valence band location. Consequently, these changes significantly influenced the EC and PEC performance of electrodeposited materials.

2. Experimental details

The Cu-Cu_2O-rGO composite films were electrodeposited from an electrolyte prepared by dissolution of 0.4 M Cu^{2+} (Avantor Materials, $CuSO_4$, analytically pure), 3 M lactic acid (Avantor Materials, analytically pure,), and addition of 1 g/L rGO (< 18 % O, < 20 μm) (Advanced Graphene Products, Poland). 8 M NaOH solution was utilized for adjustment of pH to 9.5. Before electrodeposition electrolyte was kept in ultrasonic cleaner for 15 min.

Electrodeposition was performed in a standard three-electrode system with a platinum gauze counter electrode, Ag/AgCl leakless reference electrode. Glass coated with indium tin oxide (ITO) (Ossila Ltd., unpatterned, 25 mm×25 mm, thickness 1.1 mm,40 Ω;) was applied as the working electrode. Electrodeposition was performed at room temperature for 1 h.

ITO substrates before deposition were sonicated for 5–10 minutes in hot distilled water and Hellmanex-III (1 ml of Hellmanex-III in 100 ml of water), then sonicated in hot distilled water for 5 minutes. After the sonification substrate was rinsed with distilled water and again sonicated for 5 min in isopropyl alcohol. After rinsing with distilled water substrate was dried with the air gun. The dried ITO substrate was then cleaned in plasma cleaner for 20 min.

Electrodeposition, EIS measurements, and catalytic performance of obtained layers were conducted with the use of Biologic SP-200 potentiostat/galvanostat with the EIS module. The instrument was controlled using EC-Lab software (v11.20).

XRD patterns were recorded using a Panalytical Empyrean diffractometer (Cu anode, 40 mA, 40 kV) in the 2theta range from 20 to 80 deg (step of 0.0263 deg, scan rate of 0.2 deg min^{-1}).

Observations of the layer's morphology were performed using a scanning electron microscope (Quanta 3D 200i) in SE mode (10 kV, magnification of 10k).

Mott-Schottky plots were recorded using a standard three-electrode system composed of Cu-Cu_2O-rGO@ITO working electrodes, a leakless Ag/AgCl reference electrode, and a Pt gauze counter electrode. Measurements were performed in the dark in 0.1 M $KHCO_3$ (Ar purged for 15 min, pH = 9.03) at a frequency of 1 kHz with an amplitude of 15 mV.

The potentials corresponding to Mott-Schottky results were presented versus the reversible hydrogen electrode (RHE):

$$E_{RHE} = E_{Ag/AgCl} + 0.0592 \cdot pH + E^{\circ}_{Ag/AgCl} \quad (1)$$

where: E_{RHE} – potential vs RHE, $E^{\circ}_{Ag/AgCl} = 0.197$ V (25°C), and $E_{Ag/AgCl}$ – the potential vs RE.

Diffuse reflectance spectroscopy measurements were conducted using a PerkinElmer UV-Vis-NIR Lambda 750 spectrometer (100 mm-integrating sphere, InGaAs detector) with Spectralon® as the reference sample.

Photoelectrocatalytic and electrocatalytic performance was analyzed using a customized photoelectrochemical flow cell (Zahner, optical window diameter of 18 mm) at potentiostatic conditions.

Xe lamp (150 W, Horiba) was utilized as the light source in photoelectrochemical measurements. Measurements were performed in a three-electrode system with Nafion 117 membrane separating catholyte and anolyte (Fuel Cell Store). Nafion membrane was activated using the following procedure: a) immersion in 3 % H_2O_2 (80°C, 1 h), b) immersion in deionized water (80°C, 2 h), c) immersion in 0.5 M H_2SO_4 (80°C, 2 h), and d) immersion in deionized water (80°C, 2 h). The membrane was rinsed with distilled water between the boiling steps and after the final boiling step. After the pretreatment, the membranes were stored in deionized water.

Catalytic tests were conducted in 0.1 M $KHCO_3$ saturated with CO_2 (pH = 6.80). Cu-Cu_2O-rGO@ITO working and leakless Ag/AgCl reference electrodes were located in the cathodic chamber while platinum gauze counter electrode in the anodic one.

The flow rate of electrolytes was kept at 50 ml/min using a Totton Flojet HPR 6/8 pump. The flow was controlled using an ultrasonic flowmeter (Flowmax 42I, AEA Technique). The constant electrolytes temperature was kept at 25 °C (IKA HRC 2 Control thermostat). Catholyte supplying the flow cell was continuously saturated with CO_2 (99.9999 %, Air Liquide) in the reservoir (500 ml) supplied with an aeration diffuser. The flow of CO_2 used for electrolyte saturation was kept at a flow of 50 ml/min with the use of a mass flow controller (MFC) (Bronkhorst F201CV-1K0).

Gas chromatography (GC-MS/TCD, Shimadzu QP2020) equipped with HP-PLOT/U column for MS line (0.530 mm diameter, 30 m length, Agilent, J&W; helium carrier gas flow rate of 377.5 ml·min^{-1}) was utilized for determination of the concentration of particular products in syngas. The analyses were performed at 35 °C and the system was kept at 150 °C for 600 s before each measurement. The composition of syngas was determined using certified calibration mixtures (Air Liquide, Poland).

The XPS analyses were carried out in a PHI VersaProbeII Scanning XPS system using monochromatic Al Kα (1486.6 eV) X-rays focused to a 100 μm spot and scanned over the area of 400 μm x 400 μm. The photoelectron take-off angle was 45° and the pass energy in the analyzer was set to 46.95 eV (0.1 eV step) to obtain high energy resolution spectra for the Cu $2p_{3/2}$ region. A dual beam charge compensation with 7 eV Ar^+ ions and 1 eV electrons was used to maintain a constant sample surface potential regardless of the sample conductivity. All XPS spectra were charge referenced to the unfunctionalized, saturated carbon (C-C) C 1 s peak at 285.0 eV. The operating pressure in the analytical chamber was less than 3.0×10^{-9} mbar. Deconvolution of spectra was carried out using PHI MultiPak software (v.9.9.3). Spectrum background was subtracted using the Shirley method.

For X-ray absorption spectroscopy (XAS) measurements, the samples were scraped from electrodes and then ground with mortar and pestle. Then, they were spread on adhesive Kapton tape and attached to the stainless steel frame, while the excess of the material was removed using cotton buds. The spectra at the Cu K-edge were collected at the bending magnet ASTRA beamline [59] of the National Synchrotron Radiation Centre SOLARIS [60]. The measurements were made in transmission mode using an incident photon beam provided by a modified Lemonnier type double crystal monochromator equipped with a Ge(220) crystal pair as monochromators. Three consecutive scans for each sample were processed and analyzed using the ATHENA program from the DEMETER software package [61]. The energy calibration and alignment of the collected spectra were made based on Cu foil reference spectra. It was

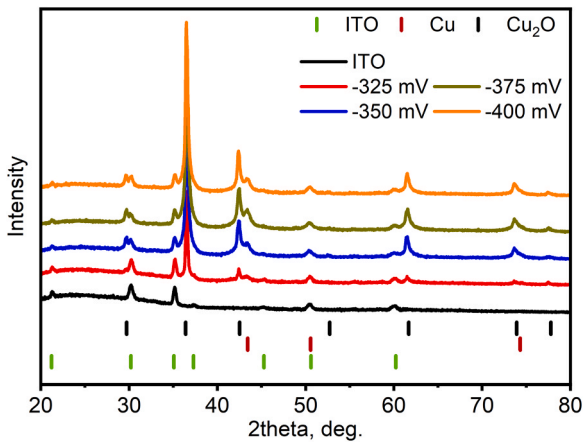

Fig. 1. XRD patterns for Cu-Cu_2O-rGO@ITO composite coating electrodeposited at various $E_{dep.}$ (vs. Ag/AgCl).

recorded before and during the sample scans in the reference chamber, with the absorption edge of 8979 eV (read as the first maximum of the spectrum derivative).

3. Results and discussion

Cu-Cu_2O-rGO composite layers were electrodeposited using a potential range determined based on results describing the mechanism of electrode reactions resulting in the formation of Cu-Cu_2O composite films reported by Mech et al. [30,62]. Cu-Cu_2O-rGO composite materials were deposited on the ITO substrate by applying electrodeposition potentials of – 325, – 350, – 375, and – 400 mV (vs Ag/AgCl). During the electrodeposition, rGO flakes were co-deposited and incorporated into the composite layer.

Fig. 1 shows XRD patterns for ITO and for electrodeposited Cu-Cu_2O-rGO composite layers. Independently on deposition potential, there are visible peaks corresponding to the presence of metallic copper and cuprite phases (International for Diffraction Data (ICDD); ICDD:98–062–7117, ICDD:98–005–3322). It may be observed that peaks existing in the XRD pattern for ITO substrate (ICDD: 98–005–0849) are also visible in spectra recorded for composite films. It was observed that peaks corresponding to the ITO located at 2theta = 37.29, 35.08, and 30.16 deg and to Cu_2O, existing in the same angle range overlap. The subsequent peak corresponding to ITO existing at 50.57 deg appears in an angle range very close to location of the peaks characteristic to metallic Cu. It is visible that with the decrease of the deposition potential, the intensities of peaks corresponding to the copper and cuprite presence increase while peaks coming from the ITO substrate decrease. These changes in the spectra indicated an increase in layer thickness with deposition potential decrease and that the electronegativity of the WE may be considered as the main factor affecting the kinetics of electrode processes. Comparing the XRD patterns presented in this work to those obtained previously for Cu-Cu_2O layers it may be concluded that the presence of rGO in the electrolyte results in changes in the kinetics of reactions resulting in the formation of Cu and Cu_2O phase as well [30]. The presence of rGO resulted in significant differences in the intensity of peaks corresponding to Cu_2O existing at 36.43 deg, 42.49 deg., and 61.7 deg. as well as to metallic Cu phase existing at 43.41 deg. In Cu-Cu_2O composite layers the intensity of peak coming from the Cu_2O phase visible at 42.49 was higher than this corresponding to metallic Cu (43.41 deg.) only for $E_{dep.}$ of – 400 mV. For remaining $E_{dep.}$ the effect was opposite and the intensity of the peak coming from metallic Cu was higher, indicating a higher amount of Cu present in the layer. For the Cu-Cu_2O-rGO composite layer independently of applied electrodeposition potential the peak related to Cu_2O existing at 42.49 deg. was higher than the peak related to Cu visible at 43.41 deg. It was also observed that the intensity of the peak existing at 36.43 deg. Corresponding to the Cu_2O phase is much higher for Cu-Cu_2O-rGO than for Cu-Cu_2O layers deposited at the same $E_{dep.}$ values. Observed significant differences in recorded XRD patterns indicated the presence of rGO in the electrolyte favouring the formation of the Cu_2O phase during the electrodeposition process [30].

Although in the XRD patterns, there are no peaks related to the presence of rGO in electrodeposited layers its existence was revealed by results of SEM layers morphology observations (Fig. 1, Fig. 2). On the surface of the materials, rGO flakes partially or completely covered with copper and copper oxide can be observed. SEM results indicated that electrodeposited layers morphology is dependent on applied deposition potential. The surface of the Cu-Cu_2O-rGO layer deposited at $E_{dep.}$ = – 325 mV consists of a flat area covered with a Cu-Cu_2O layer and spherical Cu-Cu_2O crystallites. There are also visible rGO flakes attached to the electrode surface and also covered with a copper-cuprite layer.

At lower electrodeposition potential of – 350 mV the formation of polyhedral Cu_2O crystallites and cauliflower-like structures was observed. Independently on applied deposition potential, in the films, there are visible rGO flakes decorated with Cu-Cu_2O. Further decrease of the electrodeposition potential caused a slight increase in the size of polyhedral Cu_2O crystallites and a larger amount of cauliflower-like structures.

The formation of similar Cu_2O crystallites at ITO substrate was reported also in our previous work dedicated to the properties of electrodeposited Cu-Cu_2O composite films [30]. The formation of similar octahedral Cu_2O structures formed in copper lactate-based electrolytes of higher temperature (60 °C) onto the surface of Al substrate at lower potentials, close to – 300 mV (Ag/AgCl) was also observed by Du et al. [63]. SEM analysis showed that the phase composition and morphology of electrodeposited coatings are strongly affected by the presence of rGO influencing the kinetics of electrode reactions and thus phase composition of electrodeposited composite layers. As was indicated by SEM images presence of rGO affected also the distribution of electrodeposited Cu and Cu_2O phases increasing electrochemically active surface area (EASA) and providing the possibility of the existence of a larger amount

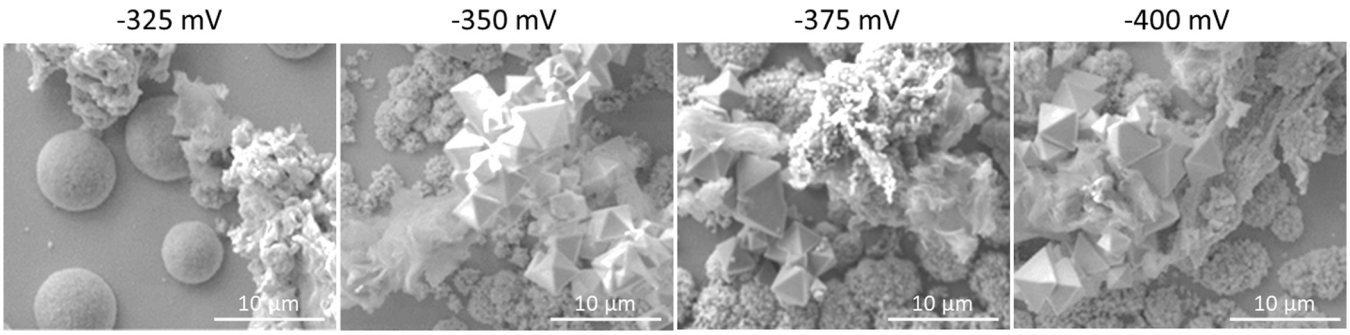

Fig. 2. SEM images of Cu-Cu_2O-rGO@ITO composite layers electrodeposited at different $E_{dep.}$ (vs Ag/AgCl) (mag. 10k).

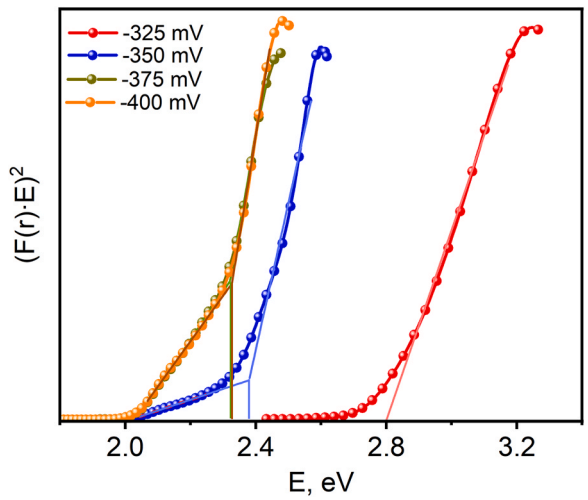

Fig. 3. Tauc plots derived from DRS spectra of layers deposited at varying $E_{dep.}$.

of catalytically active sites. SEM images along with recorded XRD patterns show the value of applied $E_{dep.}$ and the presence of rGO are important in terms of modulation of the Cu/Cu_2O phase ratio which is considered to be crucial in terms of the selectivity of electrodeposited layers [27,64]. All the above-mentioned factors are considered especially important in electrochemical and photoelectrochemical CO_2 conversion.

An effect of the electrodeposition potential on band gap width was investigated based on Tauc plots derived from collected DRS spectra presented in Fig. 3. The dependences were plotted based on the Tauc equation:

$$(\alpha \cdot h\nu)^{\frac{1}{n}} = A(h\nu - E_g) \tag{2}$$

where h denotes Planck's constant, ν is the photon frequency, A represents the proportionality constant, α is the absorption coefficient, and E_g is the energy corresponding to the band gap. DRS spectra were transformed using the Kubelka-Munk function described as:

$$F(R) = \frac{(1-R)^2}{2R} \tag{3}$$

where R represents reflectance. Assuming that $F(R)$ is proportional to the absorption coefficient, α was replaced with $F(R)$. Considering the direct band gap of Cu_2O [65] (direct transition, $n = ½$), the final equation may be defined as:

$$(F(R) \cdot h\nu)^2 = A(h\nu - E_g) \tag{4}$$

The results showed that variations in electrodeposition potential led to significant changes in the band gap width, which ranged from 2.80 to 2.32 eV.

The most noticeable reduction of band gap width from 2.80 to 2.38 eV was indicated for changes in electrodeposition potential from – 325 mV to – 350 mV. It may be observed that also changes in morphology corresponding to this potential change are the most visible. A further change in electrodeposition potential from – 350 mV to – 375 mV resulted in a much lower reduction of band gap value by 0.06 eV. It is visible that there is no difference in band gap energy determined for Cu-Cu_2O-rGO layers deposited at – 375 mV and – 400 mV. Jiang et al. reported that in Cu-Cu_2O composite layers the band gap value is affected by the amount of metallic copper present in obtained deposits [66]. A decrease in deposition potential may create more preferential conditions for direct electroreduction of copper lactate complexes to copper or reduction of previously deposited Cu_2O than for the formation of cuprite [62]. Thus as indicated by XRD patterns visible

Table 1
The band gap (E_g) and flat band potential (E_{fb}) for layers deposited at varying $E_{dep.}$

$E_{dep.}$, mV (vs Ag/AgCl)	E_g, eV	E_{fb}, V (vs RHE)	$\frac{2}{\varepsilon\varepsilon_0 e N_A}$
– 325	2.80	1.49	$4.986 \cdot 10^{-4}$
– 350	2.38	1.37	$2.822 \cdot 10^{-4}$
– 375	2.32	1.25	$8.523 \cdot 10^{-4}$
– 400	2.32	1.20	$2.817 \cdot 10^{-4}$

in Fig. 1 the Cu/Cu_2O ratio increases with a decrease in electrodeposition potential which in turn may be responsible for observed changes in band gap values. It may be also seen that the intensities of peaks related to the presence of Cu and Cu_2O are very close which is reflected by very similar energies corresponding to the band gap. It was also reported that the presence of polyhedral Cu_2O structures (Fig. 2) may enhance reflectivity and simultaneously reduce light dispersion [67]. This effect may in turn contribute to the reduced visible light absorption of Cu_2O deposited by applying relatively more electronegative potentials [68].

We observed that ternary Cu-Cu_2O-rGO exhibit higher band gap values than reported previously in Cu-Cu_2O composite layers deposited at the same conditions [30]. The presence of rGO resulted in the increase of band gap value even by 0.5 eV ($E_{dep.}$ = – 325 mV) while for more electronegative deposition potentials band gap was ca. 0.3 eV higher. The energies corresponding to the band gap determined for obtained layers are summarized in Table 1.

Mott-Schottky plots presented in Fig. 4 indicated that all electrodeposited Cu-Cu_2O-rGO layers are p-type materials. In this case, the flat band potential (E_{fb}) corresponds to the position of the maximum of the valence band. The imaginary component of impedance (Z_{im}) allows the calculation of the space charge region capacitance (C_{sc}) given by:

$$C_{sc} = \frac{-i}{2\pi f Z_{im}} \tag{5}$$

where f represents the frequency of the AC signal and i represents the imaginary unit. The capacitance-voltage relationship for p-type semiconductors, based on the Mott-Schottky approximation, is expressed as:

$$\frac{1}{C_{sc}} = \frac{-2}{\varepsilon\varepsilon_0 e N_A A^2}\left(E - E_{fb} + \frac{kT}{e}\right) \tag{6}$$

Where E represents applied potential (V), T is the temperature (K), e represents the elementary charge ($1.602 \cdot 10^{-19}$ C), N_A represents the acceptor concentration (cm^{-3}), ε is the dielectric constant, ε_0 is the vacuum permittivity ($8.85 \cdot 10^{-12}$ F/m), A – is the electrode area (cm^2), and k is the Boltzmann constant (1.38×10^{-23} J/K). The donor density may determined from the slope of the Mott-Schottky plot, while the E_{fb} may be obtained by extrapolating the plot to $C = 0$.

Determined flat band potentials indicated that a increase in the electrodeposition potential results in an elestropositive shift of the flat band potentials. Most noticeable shifts were observed for the changes in the electrodeposition potential from – 325 to – 350 mV and from – 350 to – 375 mV where flat band potential was decreased by 0.12 V. Less meaningful difference of 0.05 V was observed for further change in electrodeposition potential from – 375 mV to – 400 mV.

It may be also observed that the slope of the Mott-Schottky plot expressed by $\frac{2}{\varepsilon\varepsilon_0 e N_A}$. The term is strongly dependent on synthesis conditions indicating different charge carrier densities in deposited layers (Table 1). Analyzing determined slopes it may be pointed out that composite layers deposited at – 325 and – 350 mV exhibit the highest charge carrier concentration. Flat-band potentials as well as Mott-Schottky slopes are summarized in Table 1.

Fig. 5 shows an energy diagram presenting possible charge transfer mechanisms for synthesized catalytic layers. The diagram provides a detailed representation of the band structure of all electrodeposited

Table 2
Faradaic efficiencies of Cu-based materials designed for CO_2 conversion.

Material	Synthesis method	Electrolyte	Type of reactor	FE	Conversion potential, V	Ref.
Cu–Cu_2O–rGO	Electrodeposition from Cu(II) lactate electrolyte with rGO at pH 9.5	0.1 M $KHCO_3$ (CO_2-sat.)	Modified Zahner PEC flow cell	CH_4: 10 %, C_2H_4: 9.91 % CO: 20.84 %	– 0.6 to – 1.1 V vs. RHE	This work
Cu-Cu_2O	Electrodeposition from Cu(II) lactate electrolyte at pH 9.5	0.1 M $KHCO_3$ (CO_2-sat.)	Modified Zahner PEC flow cell	CH_4: 13.37 %, C_2H_4: 8.99 % CO: 16.27 %	– 0.6 to – 1.1 V vs. RHE	[30]
ER-Cu_5-LDH/rGO	Co-precipitation of Cu_5Al-CO_3 LDH with GO, electrochemical reduction	0.1 M $KHCO_3$ (CO_2-sat.)	H-type cell	C_2H_4: 54 %	– 1.2 V vs. RHE	[69]
ER-Cu_2O/rGO	Physical mixing of Cu_2O with GO, sonication, electroreduction	0.1 M $KHCO_3$ (CO_2-sat.)	H-type cell	C_2H_4: 27 %	– 1.2 V vs. RHE	[69]
CuO/Cu_2O NWAs@rGO	Thermal oxidation (600°C, 4 h), self-assembly of rGO	CO_2 + H_2O (gas phase)	Gas-closed reactor	CO: 0.31 μmol/cm^2 (24 h)	Photocatalysis (no bias)	[70]
NG/Cu	Spray of Cu_2O NPs on nitrogen-doped graphene (NG) on GDE	1 M KOH	Flow cell	C_{2+} (mainly ethanol): 68 %	– 1.4 V vs. RHE	[71]
BG/Cu	Spray of Cu_2O NPs on boron-doped graphene (BG) on GDE	1 M KOH	Flow cell	CO: 64.2 %	– 1.4 V vs. RHE	[71]
rGO/Cu	Spray of Cu_2O NPs on rGO on GDE	1 M KOH	Flow cell	CO: 88.2 %	– 1.4 V vs. RHE	[71]
PVA/rGO/(Cu_2O/Cu_Cl)	Cu_2O nanocubes via reduction with ascorbic acid, halide-assisted size control, rGO + PVA, film casting	0.5 M $KHCO_3$	Sealed 2 ml vessel	Methanol: 63 %	– 0.75 V vs. RHE	[72]
Cu–Cu_2O–CeOx/rGO	Electrostatic adsorption of Cu^{2+} and Ce^{3+} on GO, solvothermal reaction with thiourea in EG	2 M KOH	Flow cell	C_2H_4: 32 % EtOH: 26 % AcOH: 13.5 % PrOH: 3 %	– 0.9 V vs RHE	[73]
Cu–Cu_2O/rGO	Electrostatic assembly of CHNs and GO, drop-casting, in situ electrochemical reduction to Cu–Cu_2O	1 M $KHCO_3$	Flow cell	C_2H_4: 55.4 %–68.2 % C_2H_6: 37.6 %–10.2 %	– 1.3 to – 1.4 V vs SHE	[58]
Cu–N–G	Deposition of N-doped graphene (N-G) layer on Cu foam via in situ growth (annealing + doping)	0.1 M $KHCO_3$	H-type cell	Ethanol: 33.1 %	– 0.8 V vs RHE	[9]
Cu@Cu_2O	Thermal reduction of $Cu(OH)_2$ in H_2/Ar at 250 °C → air oxidation at room temp. for 3 weeks	0.1 M $KHCO_3$	H-type cell	C_2H_4: 21 %, Ethanol: 29 %	– 1.0 V vs RHE	[29]
Cu_2O/RGO (2:1)	Modified Hummer's method, chemical reduction to rGO, in situ growth of cubic Cu_xO via wet chemistry	0.1 M $KHCO_3$	Three-electrode cell	CO: 50 %, $HCOO^-$: 18 %	– 0.9 V vs RHE	[57]
Cu_5Al-ER	Co-precipitation of Cu_5Al-LDH, calcination (LDO), in situ electrochemical reduction	0.2 M $KHCO_3$ (CO_2-sat.)	H-type cell	C_2H_4: 36 %	– 1.2 V vs RHE	[74]
CuNPs/rGO	Co-reduction of Cu(II) and GO using hydrazine in NaOH at 70 °C (drop-cast on glassy carbon)	0.1 M NBu_4PF_6 in acetonitrile	Three-electrode cell	CO and $C_2O_4^{2-}$ (no FE explicitly given)	– 1.2 to – 1.4 V vs. NHE	[75]
Cu/Cu_2O@NG	Electroreduction of MOF−199 and N-doped graphene (4:1 mass ratio) in 0.2 M KI	0.2 M KI (CO_2-sat.)	Flow cell	C_2–C_3 products: 56 % (EtOH, C_2H_4, n-PrOH)	– 1.9 V vs RHE	[76]
Cu/Cu_2O	Cu NPs mixed with CuI reconstructed via cyclic voltammetry in 1.0 M KOH	1.0 M KOH	H-type cell	C_2H_4: 28 % EtOH: 22 % PrOH: 8 %	– 0.76 V vs RHE	[77]
pCu/CuxO.GO(PtRod)	DC electrophoresis: Cu rod anode + Pt cathode in TSC & GO solution	0.1 M $TBABF_4$ in acetonitrile	Single-compartment gas-tight cell	CO: 40 % C_2H_6: 4 %	–0.28 V vs NHE	[77]
N–NiZnAl CLDH/RGO	Urea-assisted microwave synthesis of NiZnAl–LDH/RGO, calcination under NH_3 at 500 °C for 3 h	0.5 M NaCl (CO_2-sat.)	Gas-tight cell	CO: 92 %	– 0.83 V vs RHE	[78]
Ag/Cu_xO@rGO/Mo + $BiVO_4$ photoanode	Electrodeposition Cu_xO@rGO layers on the Mo-loaded FTO glass, then magnetron sputtering of Ag	0.1 M $KHCO_3$	Standalone tandem two-electrode photoelectrochemical cell	H_2: 34.1 % CO: 49.1 % CH_4: 13.0 % Formate: 0.68 %	Photocatalysis (no bias)	[79]

layers in relation to the redox potentials associated with reactions that produce liquid or gaseous products in CO_2-saturated $KHCO_3$. Obtained results indicate that CB for the layer deposited at – 325 mV is located at much more electronegative potential than it was observed for the remaining layers. However, for all electrodeposited layers redox potentials corresponding to reactions resulting in gas/liquid products formation are located at more electropositive potentials than CB edge creating the possibility of reduction of CO_2 molecules by electrons generated by incident light. Among the reactions resulting in the formation of CO_2 derivative products, the course of the reaction resulting in the formation of hydrogen is also possible. This concurrent accompanying reaction results in a decrease in selectivity and Faradaic efficiency related to conversion process. Instead of all electrodeposited layers exhibiting appropriate band location, there are many other factors strongly influencing the efficiency of the reduction of CO_2 molecules with photogenerated electrons including charge carriers recombination effect, charge separation, and light conversion efficiency as well.

Comparing the results described by Mech et al. related to the synthesis of the Cu-Cu_2O composite layers using the same procedure it may be observed that modification of the Cu-Cu_2O composite layer with rGO results in a much more different band structure. Modification of the Cu-Cu_2O composite layer with rGO resulted in a significant shift of the flat band potential towards the electropositive direction. The most significant shift resulting from the presence of rGO was observed for the layer deposited at – 350 mV and it was 0.3 V. The presence of rGO resulted also in a much wider band gap width. The band gap width increased even by 0.5 eV for layers deposited at – 325 mV. Although, differences in E_{fb} location and E_g were noticeable for layers deposited at $E_{dep.} \leq$ –

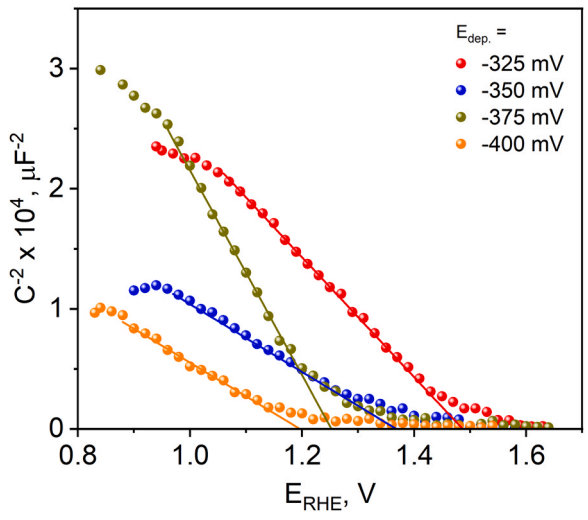

Fig. 4. Mott-Schottky plots for films deposited at various $E_{dep.}$ (0.1 M $KHCO_3$ purged with Ar for 15 min A = 15 mV, f = 1 kHz).

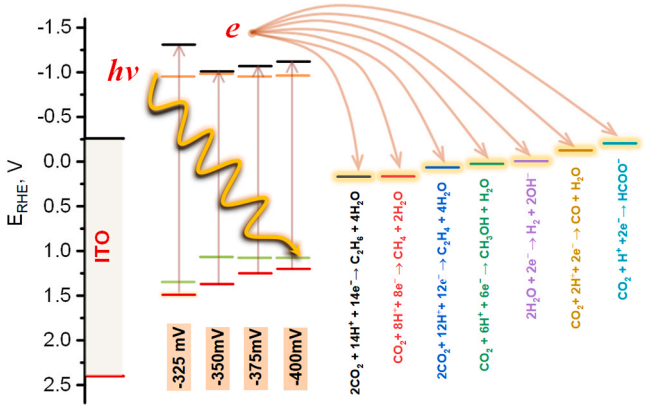

Fig. 5. The energy diagram based on determined E_g and E_{fb} values with reactions involved in the reduction of CO_2 to gaseous products in $KHCO_3$. (green lines: VB of Cu-Cu_2O, orange lines: CB of Cu-Cu_2O, [30]).

350 mV the VB edge was located in similar potentials as it was in the case of Cu-Cu_2O composite layers. The only noticeable difference was observed between layers deposited at – 325 mV, hereafter modification of the layer surface with rGO the CB was significantly shifted towards electronegative direction by 0.36 V. Previous studies suggest that Cu vacancies play a crucial role in enhancing the catalytic activity of Cu_2O for photoelectrochemical CO_2 reduction. Additionally, it was observed that the concentration of these Cu vacancies, as well as holes in Cu_2O, can be effectively controlled by adjusting the deposition potential [80].

Consistent with our findings, it has been observed that modifying electrodeposition conditions enables the synthesis of materials with varying conduction band (CB) and valence band (VB) positions, directly influencing their photoelectrochemical activity. This highlights that the overall performance of light-driven CO_2 conversion using composite materials arises from the complex interplay of multiple factors, each playing a crucial role in photoelectrocatalytic activity.

Also, DFT calculations have shown that both tensile and compressive strain in the cuprite crystal lattice can significantly reduce the band gap of Cu_2O [81]. Electrodeposition depending on current-voltage conditions may also generate internal stresses in deposited layers [82–84]. It was observed that tensile stress tends to dominate in thin copper films deposited at high overpotentials, whereas compressive stress becomes more prominent in thicker films [82]. Apart from internal stresses and defect density, there are also other factors strongly affecting the final properties of deposited films including among others bath composition, overpotential, current density, temperature, agitation, substrate material, and film thickness. Voltammetric and electrogravimetric results reported in the literature demonstrate that varying the electrodeposition potential of Cu-Cu_2O significantly influenced the kinetics of electrodeposition processes [62]. The kinetics of electrode reactions and the mechanism of film growth may be considered as key factors affecting the final properties of electrodeposited films including the conduction band (CB), valence band (VB) location, and the band gap value as well. Thus proper adjustment of electrodeposition parameters creates possibilities for the synthesis of layers of properties adjusted in terms of specific applications.

The highest value of E_g in the case of Cu-Cu_2O-rGO layer deposited at – 325 mV amounting to 2.8 eV may result in limited light absorption and a lower concentration of photoinduced electrons in the conduction band. A decrease of $E_{dep.}$ resulting in a decrease of the band gap value to less than 2.4 eV significantly enhancing light absorption efficiency. The decrease of the band gap value may simultaneously result in an enhanced photogenerated charge recombination effect. Instead of significant shifts of E_{fb} toward less electropositive direction resulting from applied $E_{dep.}$ the conduction band is still located at more electronegative potentials than the redox potential characteristic for reactions in which CO_2 is reduced to several added-value species creating possibilities of utilization of electrodeposited layers in light-supported reduction of CO_2. Overall enhancement of photoelectrocatalytic CO_2 reduction is also dependent on the kinetics and mechanism of the charge transfer processes at several interfaces existing in Cu-Cu_2O-rGO composite layers. The presence of metallic Cu catalyzing CO_2 reduction directly may also reduce the charge transfer recombination effect due to the formation of the Schottky barrier at the Cu_2O/Cu interface. Location of the Fermi level of Cu (WF = 4.7 eV, [85]) at less electropositive potential than the Fermi level of Cu_2O (WF = 4.32–4.66 eV, [86]) supporting the transfer of the electrons from the conduction band of Cu_2O to metallic copper. A similar effect resulted in unidirectional electron transfer from the Cu_2O conduction band existing at the Cu_2O/rGO interface. Mutual Fermi level location of rGO (WF = 4.8 eV, [87]) and Cu_2O and high conductivity of rGO driving transportation of the electrons to surface-active sites or metallic Cu. Presence of rGO limiting recombination effect, supporting charge transfer and enhancing surface reactions kinetics. The presence of rGO resulting in also in an enlarged surface area creating preferential conditions for CO_2 molecules adsorption and their further reduction. The existence of Cu/rGO interfaces at highly developed rGO surface may also enhance charge transport and its redistribution across the surface of Cu providing appropriate conditions for the formation of numerous catalytically active sites.

EC and PEC tests were conducted in CO_2-saturated 0.1 M $KHCO_3$ at potentials ranging from – 0.6 to – 1.1 V (vs RHE) (each 0.1 V). The concentration of gaseous products in syngas was determined using gas chromatography. The Faradaic efficiency was calculated using the following equation:

$$FE = \frac{V_n \cdot z_n \cdot F \cdot p}{Q \cdot R \cdot T} \cdot 100\% \quad (7)$$

where F represents the Faraday constant, Q is the charge, p is the pressure, R is the gas constant, T is the temperature, V_n is the volume of the collected n gas (CH_4, C_2H_4, C_2H_6), z_n is the number of electrons characteristic for particular products (z_n = 2, 8, and 12 for CO, CH_4, and C_2H_4, respectively).

The effect of illumination on the changes in *FE* for particular gas products was described by dependence expressing the ratio of the *FE* determined for the layer tested under illumination to *FE* determined for the layer tested in the dark:

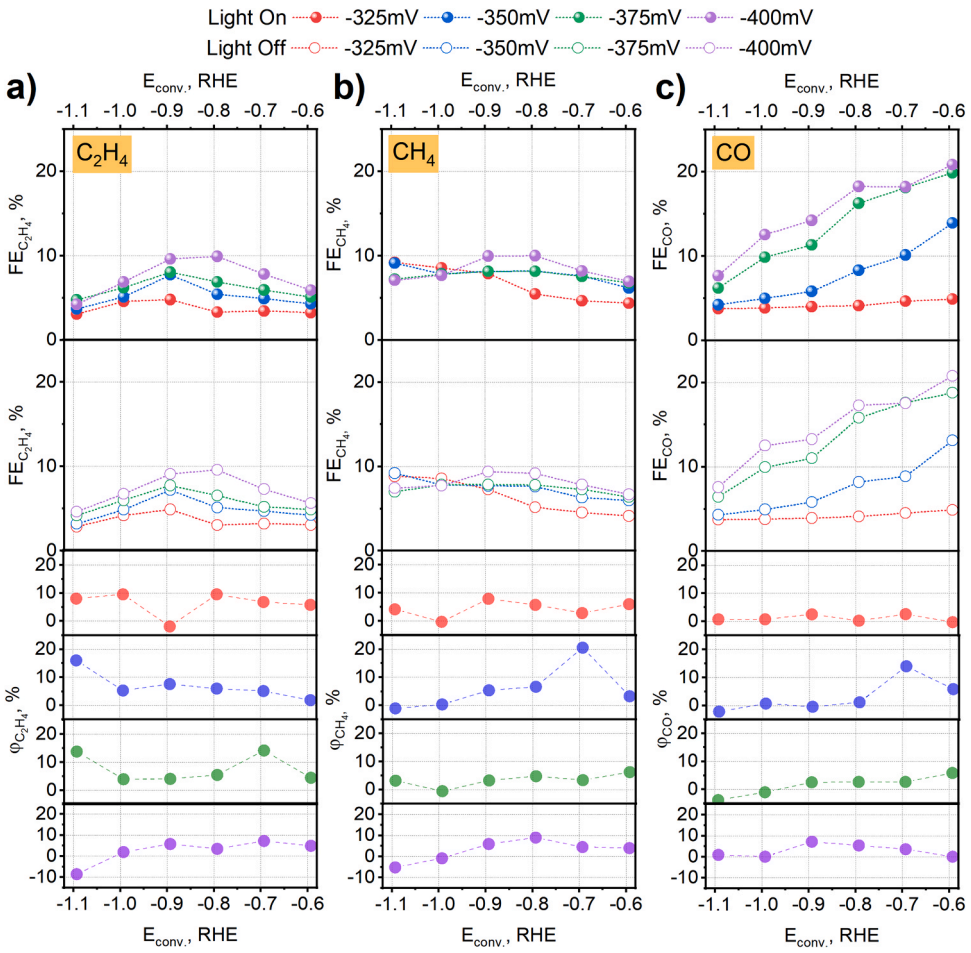

Fig. 6. FE and φ factor calculated for a) C_2H_4, b) CH_4, and c) CO. FEs were calculated for all electrodeposited layers tested at various $E_{conv.}$ at dark and under light illumination.

$$\varphi = \frac{Q_{LightOn}}{Q_{LightOff}} \cdot 100\% \quad (8)$$

The dependences representing the differences resulting from the illumination are presented in Fig. 6a), b), and c) (bottom part) for C_2H_4, CH_4, and CO, respectively. It should be also mentioned that syngas contained significant amounts of hydrogen resulting from the course of concurrent hydrogen evolution reaction.

The partial current efficiencies (*FE*) for particular gaseous products obtained in the dark and under illumination are shown in Fig. 6. Results of GC-MS/TCD analyses revealed the presence of CH_4, C_2H_4, CO, and H_2 in syngas. Independently on the applied conversion potential the *FE* for H_2 was significantly higher than for remaining gas products and ranging from 59.02 % ($E_{conv.}$ = – 0.9 V, $E_{dep.}$ = – 400 mV, Light Off) to 79.07 % ($E_{conv.}$ = – 1.1 V, $E_{dep.}$ = – 350 mV, Light On).

The highest values of FE for the conversion of CO_2 to C_2H_4 were observed for the Cu-Cu_2O-rGO layers synthesized at – 400 mV (Fig. 6a). The FE_{max} for ethylene production is located at – 0.8 V and amounting to 9.91 % (Light On) for the layer deposited at – 400 mV whereas for materials electrodeposited at more positive potentials, the FE_{max} shifts to – 0.9 V. The presence of light does not affect the location of the maximum related to C_2H_4 production. Independently on $E_{conv.}$ it was observed that *FE* for C_2H_4 reaches higher values with the decrease of the $E_{dep.}$ value. This effect may be related to the increasing amount of metallic copper promoting the formation of the C=C bond. The effect of illumination resulted in an increase of *FE* even by 16.09 % ($E_{dep.}$ = – 350 mV, $E_{conv.}$ = – 1.1 V). It was also observed that illumination in most cases increased *FE* except layers deposited at – 300 and – 400 mV for $E_{conv.}$ of – 0.9 and – 1.1 V, respectively (Fig. 6a, bottom). The decreased *FE* resulting from the presence of light may result from the preferential course of concurrent electrode reactions.

FE calculated for methane indicated that the highest *FE* amounting to 10 % was observed for layer deposited at – 400 mV at $E_{conv.}$ = – 0.8 V in light-supported conditions (Fig. 6). It is visible that under light illumination at $E_{conv.} \geq$ – 0.9 V *FE* for CH_4 increases with the decrease of $E_{dep.}$ except the layers deposited at – 350 and – 375 mV for which calculated Faradaic efficiencies are almost the same with a slight difference for $E_{conv.}$ of – 0.6 V. In dark conditions in this $E_{conv.}$ range the situation a slight difference in *FE* calculated for layer deposited at – 350 mV and – 375 mV is visible also at $E_{conv.}$ of – 0.7 V. At $E_{conv.} \leq$ – 1.0 V independently on light conditions the situation is different and clear dependence between $E_{dep.}$ and calculated *FE* is not observed. At $E_{conv.}$ of – 1.0 V for all applied $E_{dep.}$ *FE* are almost the same and amounting to ca. 7.65 %. What is more the illumination of the layer does not result in any changes in *FE*. It may be also observed that illumination of the layer surface at $E_{conv.} \geq$ – 0.9 V resulted in a slight increase in the *FE* ranging from 3.29 % ($E_{conv.}$ = – 0.9 V, $E_{dep.}$ = – 0.375 mV) to 20.64 % ($E_{conv.}$ = – 0.7 V, $E_{dep.}$ = – 350 mV) (Fig. 6b, bottom). For $E_{conv.}$ of – 1.0 V the effect resulting from the change in light intensity was not visible. In two cases (for $E_{dep.}$ = – 350 mV and $E_{dep.}$ = – 400 mV) at $E_{conv.}$ of – 1.1 V illumination of the layer resulted in a decrease in *FE*.

Fig. 6c presents *FE* dependences calculated for CO. It is visible that the *FE* for CO formation increases with the decrease of $E_{dep.}$. There is one exception observed for $E_{conv.}$ of – 0.7 V where calculated *FE* for layers deposited at – 375 and – 400 mV are almost the same independently on light conditions. It is also observed that the highest values of *FE* are

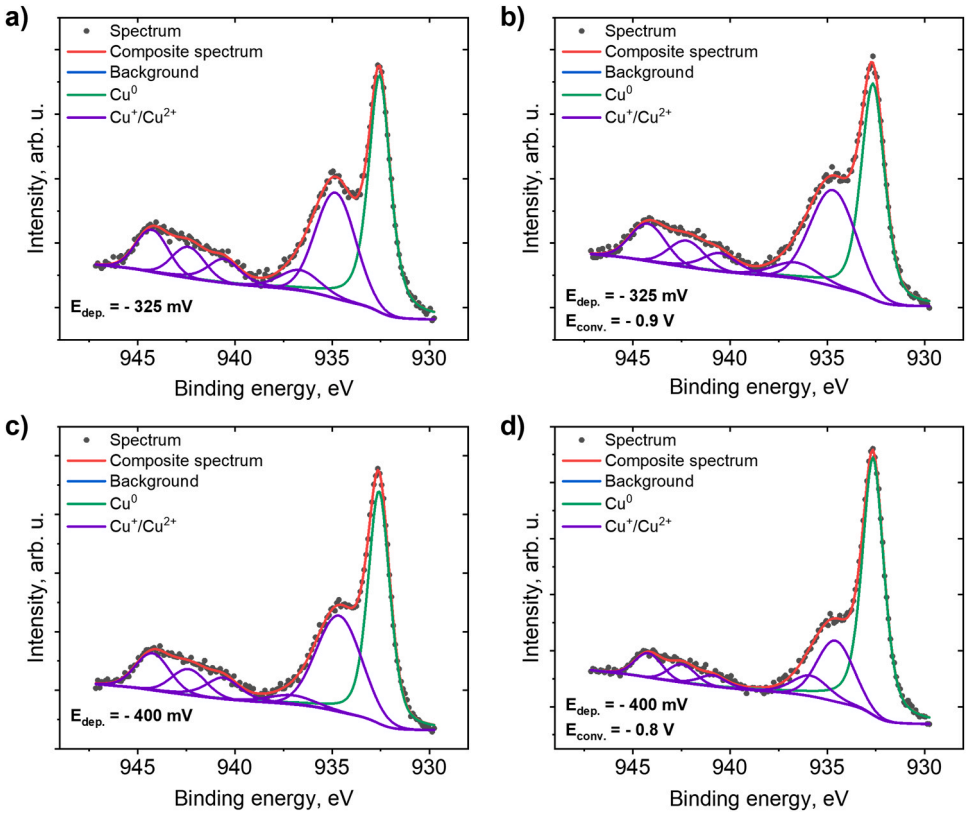

Fig. 7. Deconvolution of Cu $2p_{3/2}$ spectra for Cu-Cu_2O-rGO composite layers deposited at – 325 mV (a, b) and – 400 mV (c, d) before (a, c) and after (b, d) catalytic tests.

achieved at – 0.6 V and are decreasing with the decrease of the $E_{conv.}$ potential. Also, the differences in *FE* result from differences in $E_{dep.}$ are less meaningful with the decrease of $E_{conv.}$. The dependences reflecting the influence of layer illumination on *FE* changes indicated independently on $E_{conv.}$ only slight differences in *FE* determined for layers tested in the dark and at light-illuminated conditions. The most significant effect of the illumination was indicated for the composite layer electrodeposited at – 350 mV tested at $E_{conv.}$ of – 0.7 V.

Obtained results indicated that the presence of light slightly influences the kinetics of electrode reactions and the most important parameters that significantly affect the electrochemical performance of synthesized Cu-Cu_2O-rGO composite layer are deposition potential and conversion potential as well.

The electrochemical performance of Cu_2O cubic crystals in electrocatalytic CO_2 reduction to ethylene was also investigated by Ning et al. Authors reported a maximum *FE* for C_2H_4 of approximately 16 % at – 1.3 V (vs. RHE) [88]. Similarly, Ren et al. explored Cu_2O films, emphasizing that film thickness plays a crucial role in determining the reaction kinetics and selectivity of electrode reactions. XRD analysis revealed that the reduction of Cu_2O to metallic copper promotes the preferential formation of C_{2+} products, with this effect being more pronounced in thicker films. The highest *FE* for ethylene formation, 40.25 %, was achieved with a 0.9 μm thick film [28]. Additionally, the authors highlighted that Cu_2O electrodes exhibit significantly faster reaction kinetics compared to polished copper. This enhancement was attributed to the increased roughness caused by the reduction of Cu_2O, which enlarges the electrochemically active surface area [28]. Notably, the electrochemical performance of copper(I) catalysts was assessed within the same potential range as that used in the study by Mech et al. [30]. The authors observed that the maximum of *FE* for C_2H_4 was shifted toward more electropositive potentials (– 0.9 V vs. RHE) and indicated that maximal Faradaic efficiency for CH_4 and C_2H_4 were observed for illuminated layers and amounted to 13.37 and 8.99 %, respectively.

Table 3
Relative composition [%] derived from fitting the Cu $2p_{3/2}$ regions for Cu-Cu_2O-rGO composite layers deposited at different $E_{dep.}$ before and after (b, d) catalytic tests.

$E_{dep.}$, mV (vs Ag/AgCl)	Description	$E_{conv.}$, V (vs RHE)	Cu(0)	Cu(I)/Cu(II)
– 400	before catalytic test		44.1	55.9
– 400	after catalytic test	– 0.8	60.6	39.4
– 325	before catalytic test		39.7	60.3
– 325	after catalytic test	– 0.9	46.7	53.3

Results obtained for Cu-Cu_2O-rGO catalytic layers reported in the present work indicated lower *FE* for methane generation, amounting to 10 %. On the other hand, the FE for ethylene slightly increased by 0.92 %. Although the presence of rGO in electrodeposited layers significantly affected both band gap width and flat band location these changes do not result in noticeable changes in selectivity or Faradaic efficiencies of obtained materials. The obtained results were summarized in Table 1 and compared with catalytic performance of selected Cu-based materials.

XPS and XAS analyses were carried out to determine the changes in surface chemical states and the oxidation states of copper in the composite layers deposited at narrow $E_{dep.}$ values. The spectra were recorded before and after the catalytic test performed at light-supported conditions for samples exhibiting the highest Faradaic efficiencies of C_2H_4 formation. The XPS spectra in the Cu $2p_{3/2}$ region for the four investigated samples are shown in Fig. 7. Each of the spectra was fitted with six components, with the main peak located at a binding energy of 932.6 eV, indicating the presence of metallic copper [89,90]. A shoulder on the left side, consisting of two components positioned at 934.7 eV and 936.6 eV, corresponds to oxidized copper states in both + 1 and + 2 oxidation states – present as oxides and/or hydroxides. Additionally,

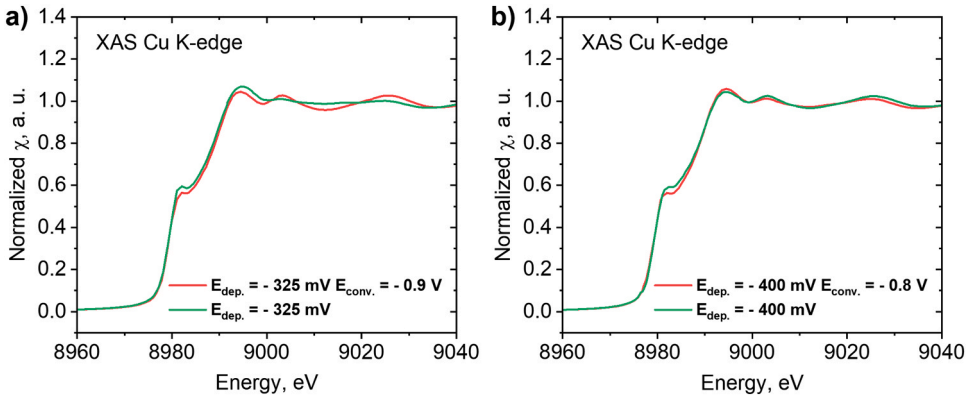

Fig. 8. XANES spectra for Cu-Cu_2O-rGO composite layers deposited at – 325 mV (a, b) and – 400 mV (c, d) before (a, c) and after (b, d) catalytic tests.

three shake-up satellite peaks in the 940–945 eV range confirm the presence of Cu^{2+} species [89,91,92]. Table 3 presents the relative contents of copper, divided into oxidized and metallic fractions. In both cases, results indicate higher amounts of metallic copper after the photoelectrocatalytic conversion of CO_2 than before. There are also differences in the surface phase composition of samples deposited at −325 mV and −400 mV which are consistent with XRD results (Fig. 1). In layers deposited at −325mV the Cu_2O/Cu ratio is higher than in layers deposited at – 400 mV. Observed results suggest instability of the electrodeposited layer and electrochemical reduction of the Cu_2O present at the surface of layers during the conversion process. XPS results are also consistent with previously reported electrochemical quartz crystal microbalance (EQCM) results (Table 3) [30].

It must be emphasized that the coexistence of multiple copper-related species and the presence of two oxidation states is a result of both the surface sensitivity of the XPS technique (in the applied measurement geometry, the analysis probes to a depth of up to 5 nm), as well as copper's natural tendency to oxidize under atmospheric conditions to form oxides and hydroxides. For these reasons, the characteristic spectrum of rGO in the C 1 s region was not observed – rGO is covered by a layer of copper and air-derived contaminants that is too thick to allow for a measurable signal.

Fig. 8a and b show the X-ray absorption near edge structure (XANES) measured for catalytic layers listed in Table 3. The entire spectra, including the extended X-ray absorption fine structure (EXAFS), are shown in Figs. S2–4. The characteristic feature at 8979 eV appears in both metallic copper and Cu_2O, but not in CuO (as shown in Figure S1). It is more pronounced for Cu_2O than for metallic Cu. For both Cu-Cu_2O-rGO catalytic layers electrodeposited at – 300 and – 400 mV we observe features characteristic of Cu and Cu_2O. The feature at 8979 eV is slightly decreasing for samples after the catalytic tests, which indicates the reduction of Cu_2O. This change is more clear for the Cu-Cu_2O-rGO composite layer deposited at – 325 mV, containing initially more Cu_2O phase which is in agreement with XRD (Fig. 1) and XPS (Fig. 7) analyses.

4. Conclusions

In this work, we reported results concerning the application of electrodeposited Cu-Cu_2O-rGO catalytic layers in electrochemical and photoelectrochemical conversion of CO_2. Obtained results indicated that the presence of rGO significantly affected E_g value and E_{fb} location compared to Cu-Cu_2O layers electrodeposited at the same condition reported in the literature. Additionally, a decrease in electrodeposition potential resulted in increased *FE* towards the formation of C_2H_4 and CO. The effect was also visible for CH_4 but in a limited potential window. Maximal Faradic efficiency toward C_2H_4 formation was observed at E_{conv} = – 0.8 V and it was 9.91 % (Light On). The location of the maximum of *FE* for CH_4 was also observed at E_{conv} = – 0.8 V and it was 10 % (Light On). Reported results indicated that both electrodeposition and conversion potential significantly affected Faradaic efficiency towards the formation of particular gas products. It was also observed that the presence of light resulted in changes in most cases resulting in the increase of *FE* for CH_4, C_2H_4, and CO formation compared to FEs obtained in the dark conditions, but at some potentials presence of light resulted in increased kinetics of concurrent electrochemical reactions related to hydrogen evolution or formation of liquid conversion products. XPS and XAS analyses confirmed the degradation of the layers during the photoelectrochemical conversion of CO_2 and the reduction of Cu_2O to metallic Cu.

CRediT authorship contribution statement

Csapó Edit: Writing – review & editing, Investigation. **Kolbusz Patrycja:** Writing – review & editing, Investigation, Visualization. **Mech Krzysztof:** Writing – review & editing, Writing – original draft, Visualization, Validation, Supervision, Resources, Project administration, Methodology, Investigation, Funding acquisition, Data curation, Conceptualization. **Marzec Mateusz:** Investigation, Visualization, Writing – original draft. **Sławek Andrzej:** Investigation, Visualization, Writing – original draft.

Declaration of Competing Interest

The authors declare the following financial interests/personal relationships which may be considered as potential competing interests: Krzysztof Mech reports financial support was provided by National Science Centre Poland. If there are other authors, they declare that they have no known competing financial interests or personal relationships that could have appeared to influence the work reported in this paper.

Acknowledgements

This work was supported by the Polish National Science Centre under grants 2023/49/B/ST8/01887 and 2017/26/D/ST8/00508. This research was partly supported by the programme 'Excellence Initiative - Research University' for the AGH University of Krakow.

X-ray absorption spectroscopy measurements were made at the PIRX beamline under the provision of the Polish Ministry and Higher Education project 'Support for research and development with the use of the research infrastructure of the National Synchrotron Radiation Centre SOLARIS' under contract no 1/SOL/2021/2.

Appendix A. Supporting information

Supplementary data associated with this article can be found in the online version at doi:10.1016/j.jcou.2025.103106.

Data availability

Data will be made available on request.

References

[1] V. Kumaravel, J. Bartlett, S.C. Pillai, Photoelectrochemical conversion of carbon dioxide (CO_2) into fuels and value-added products, ACS Energy Lett. 5 (2020) 486–519, https://doi.org/10.1021/acsenergylett.9b02585.

[2] D.R. Kauffman, J. Thakkar, R. Siva, C. Matranga, P.R. Ohodnicki, C. Zeng, R. Jin, Efficient electrochemical CO_2 conversion powered by renewable energy, ACS Appl. Mater. Interfaces 7 (2015) 15626–15632, https://doi.org/10.1021/acsami.5b04393.

[3] G. Abdi, A. Alizadeh, A. Podborska, K. Szaciłowski, K. Mech, Nanomaterials in artificial photosynthesis, Handb. Nanomater, Biomed., Environ., Food, Agric. 2 (2024) 655–683, https://doi.org/10.1016/B978-0-323-95513-3.00024-1.

[4] M. Umeda, Y. Niitsuma, T. Horikawa, S. Matsuda, M. Osawa, Electrochemical reduction of CO_2 to methane on platinum catalysts without overpotentials: strategies for improving conversion efficiency, ACS Appl. Energ. Mater. 3 (2020) 1119–1127, https://doi.org/10.1021/acsaem.9b02178.

[5] U. Ulmer, T. Dingle, P.N. Duchesne, R.H. Morris, A. Tavasoli, T. Wood, G.A. Ozin, Fundamentals and applications of photocatalytic CO_2 methanation, Nat. Commun. 10 (2019) 3169, https://doi.org/10.1038/s41467-019-10996-2.

[6] A.M. Ismail, G.F. Samu, H.C. Nguyën, E. Csapó, N. López, C. Janáky, Au/Pb interface allows the methane formation pathway in carbon dioxide electroreduction, ACS Catal. 10 (2020) 5681–5690, https://doi.org/10.1021/acscatal.0c00749.

[7] M. Bisztyga-Szklarz, K. Mech, M. Marzec, R. Kalendarev, K. Szaciłowski, In situ regeneration of copper-coated gas diffusion electrodes for electroreduction of CO_2 to ethylene, Materials 14 (2021) 3171, https://doi.org/10.3390/ma14123171.

[8] L. Berkelaar, J.V.D. Linde, J. Peper, A. Rajhans, D. Tiemessen, L.V.D. Ham, H.V. D. Berg, Electrochemical conversion of carbon dioxide to ethylene: plant design, evaluation and prospects for the future, Chem. Eng. Res. Des. 182 (2022) 194–206, https://doi.org/10.1016/j.cherd.2022.03.034.

[9] D. Zang, X.J. Gao, L. Li, Y. Wei, H. Wang, Confined interface engineering of self-supported Cu@N-doped graphene for electrocatalytic CO_2 reduction with enhanced selectivity towards ethanol, Nano Res. 15 (2022) 8872–8879, https://doi.org/10.1007/s12274-022-4698-3.

[10] K.M. Rezaul Karim, H.R. Ong, H. Abdullah, A. Yousuf, C.K. Cheng, M.M. Rahman Khan, Photoelectrochemical reduction of carbon dioxide to methanol on p-type $CuFe_2O_4$ under visible light irradiation, Int. J. Hydrog. Energy 43 (2018) 18185–18193, https://doi.org/10.1016/j.ijhydene.2018.07.174.

[11] J. Yuan, C. Gu, W. Ding, C. Hao, Photo-electrochemical reduction of carbon dioxide into methanol at $CuFeO_2$ nanoparticle-decorated $CuInS_2$ thin-film photocathodes, Energy Fuel 34 (2020) 9914–9922, https://doi.org/10.1021/acs.energyfuels.0c02009.

[12] A. Otto, T. Grube, S. Schiebahn, D. Stolten, Closing the loop: captured CO_2 as a feedstock in the chemical industry, Energ. Environ. Sci. 8 (2015) 3283–3297, https://doi.org/10.1039/C5EE02591E.

[13] E. Gong, S. Ali, C.B. Hiragond, H.S. Kim, N.S. Powar, D. Kim, H. Kim, S.-I. In, Solar fuels: research and development strategies to accelerate photocatalytic CO_2 conversion into hydrocarbon fuels, Energy Environ. Sci. 15 (2022) 880–937, https://doi.org/10.1039/D1EE02714J.

[14] E. Moioli, R. Mutschler, A. Züttel, Renewable energy storage via CO_2 and H_2 conversion to methane and methanol: assessment for small scale applications, Renew. Sust. Energ. Rev. 107 (2019) 497–506, https://doi.org/10.1016/j.rser.2019.03.022.

[15] J. Amouroux, P. Siffert, J. Pierre Massué, S. Cavadias, B. Trujillo, K. Hashimoto, P. Rutberg, S. Dresvin, X. Wang, Carbon dioxide: a new material for energy storage, Prog. Nat. Sci. -Mater. 24 (2014) 295–304, https://doi.org/10.1016/j.pnsc.2014.06.006.

[16] H.-R.M. Jhong, S. Ma, P.J.A. Kenis, Electrochemical conversion of CO_2 to useful chemicals: current status, remaining challenges, and future opportunities, Curr. Opin. Chem. Eng. 2 (2013) 191–199, https://doi.org/10.1016/j.coche.2013.03.005.

[17] A.M. Ismail, G.F. Samu, Á. Balog, E. Csapó, C. Janáky, Composition-dependent electrocatalytic behavior of Au–Sn bimetallic nanoparticles in carbon dioxide reduction, ACS Energy Lett. 4 (2019) 48–53, https://doi.org/10.1021/acsenergylett.8b01996.

[18] A.M. Ismail, E. Csapó, C. Janáky, Correlation between the work function of Au–Ag nanoalloys and their electrocatalytic activity in carbon dioxide reduction, Electrochim. Acta 313 (2019) 171–178, https://doi.org/10.1016/j.electacta.2019.05.016.

[19] N. Qiu, W. Lu, H.-Q. Wang, Manipulating local CO_2/H_2O ratio in electrocatalytic CO_2 reduction toward multi-carbon product, Rare Met. 44 (2025) 60–80, https://doi.org/10.1007/s12598-024-02919-y.

[20] Z. Sun, T. Ma, H. Tao, Q. Fan, B. Han, Fundamentals and challenges of electrochemical CO_2 reduction using two-dimensional materials, Chem 3 (2017) 560–587, https://doi.org/10.1016/j.chempr.2017.09.009.

[21] M. Jouny, W. Luc, F. Jiao, General techno-economic analysis of CO_2 electrolysis systems, Ind. Eng. Chem. Res. 57 (2018) 2165–2177, https://doi.org/10.1021/acs.iecr.7b03514.

[22] S. Zhang, C. Chen, K. Li, H. Yu, F. Li, Materials and system design for direct electrochemical CO_2 conversion in capture media, J. Mater. Chem. A 9 (2021) 18785–18792, https://doi.org/10.1039/D1TA02751D.

[23] F.-Y. Gao, R.-C. Bao, M.-R. Gao, S.-H. Yu, Electrochemical CO_2-to-CO conversion: electrocatalysts, electrolytes, and electrolyzers, J. Mater. Chem. A 8 (2020) 15458–15478, https://doi.org/10.1039/D0TA03525D.

[24] S. Wang, T. Kou, S.E. Baker, E.B. Duoss, Y. Li, Recent progress in electrochemical reduction of CO_2 by oxide-derived copper catalysts, Mater. Today Nano 12 (2020) 100096, https://doi.org/10.1016/j.mtnano.2020.100096.

[25] S. Chen, C. Ye, Z. Wang, P. Li, W. Jiang, Z. Zhuang, J. Zhu, X. Zheng, S. Zaman, H. Ou, L. Lv, L. Tan, Y. Su, J. Ouyang, D. Wang, Selective CO_2 Reduction to Ethylene Mediated by Adaptive Small-molecule Engineering of Copper-based Electrocatalysts, Angew. Chem. Int. Ed. Engl. 62 (2023) e202315621, https://doi.org/10.1002/anie.202315621.

[26] J.F. de Brito, A.R. Araujo, K. Rajeshwar, M.V.B. Zanoni, Photoelectrochemical reduction of CO_2 on Cu/Cu_2O films: product distribution and pH effects, Chem. Eng. J. 264 (2015) 302–309, https://doi.org/10.1016/j.cej.2014.11.081.

[27] R. Kas, R. Kortlever, A. Milbrat, M.T.M. Koper, G. Mul, J. Baltrusaitis, Electrochemical CO_2 reduction on Cu_2O-derived copper nanoparticles: controlling the catalytic selectivity of hydrocarbons, Phys. Chem. Chem. Phys. 16 (2014) 12194–12201, https://doi.org/10.1039/C4CP01520G.

[28] D. Ren, Y. Deng, A.D. Handoko, C.S. Chen, S. Malkhandi, B.S. Yeo, Selective electrochemical reduction of carbon dioxide to ethylene and ethanol on copper(I) oxide catalysts, ACS Catal. 5 (2015) 2814–2821, https://doi.org/10.1021/cs502128q.

[29] L. Shang, X. Lv, H. Shen, Z. Shao, G. Zheng, Selective carbon dioxide electroreduction to ethylene and ethanol by core-shell copper/cuprous oxide, J. Colloid Interface Sci. 552 (2019) 426–431, https://doi.org/10.1016/j.jcis.2019.05.073.

[30] K. Mech, A. Podborska, M. Marzec, K. Szaciłowski, C.P. de Leon, Electrodeposition of $Cu\text{-}Cu_2O$ composite films of adjustable band structure for photoelectrochemical conversion of carbon dioxide to hydrocarbons, Sustain. Mater. Technol. 41 (2024) e01000, https://doi.org/10.1016/j.susmat.2024.e01000.

[31] K. Mech, P. Zabiński, R. Kowalik, K. Fitzner, EQCM, SEC and voltammetric study of kinetics and mechanism of hexaamminecobalt(III) electro-reduction onto gold electrode 81 (2012) 254–259, https://doi.org/10.1016/j.electacta.2012.07.067.

[32] K. Mech, P. Zabiński, R. Kowalik, Analysis of rhodium electrodeposition from chloride solutions, J. Electrochem. Soc. 161 (2014) D458–D461, https://doi.org/10.1149/2.1101409jes.

[33] K. Mech, J. Mech, P. Zabinski, R. Kowalik, M. Wojnicki, Electrochemical deposition of alloys in Ru^{3+}-Co^{2+}-Cl^--H_2O system, J. Electroanal. Chem. 748 (2015) 76–81, https://doi.org/10.1016/j.jelechem.2015.04.022.

[34] K. Mech, G. Boczkal, P. Pałka, P. Zabiński, R. Kowalik, Synthesis of Co–Pd alloys by co-electroreduction of aquachloro-cobalt(II) and palladium(II) complexes, J. Solid State Electrochem. 18 (2014) 3121–3127, https://doi.org/10.1007/s10008-013-2363-1.

[35] K. Syrek, M. Jażdżewska, M. Kozieł, L. Zaraska, Room-temperature electrodeposition of Cu_2O layers and its low-temperature annealing for photoelectrochemical water splitting applications, Opt. Mater. 156 (2024), https://doi.org/10.1016/j.optmat.2024.115910.

[36] K. Syrek, M. Jażdżewska, M. Kozieł, L. Zaraska, Photoelectrochemical activity of Cu_2O electrochemically deposited at different temperatures, J. Ind. Eng. Chem. 115 (2022) 561–569, https://doi.org/10.1016/j.jiec.2022.09.002.

[37] K. Mech, M. Marzec, K. Szaciłowski, Ultrasound supported galvanostatic deposition of Zn coatings reinforced with nano-, submicro-, and micro-sic particles—weak acidic chloride baths, Materials 14 (2021), https://doi.org/10.3390/ma14113033.

[38] K. Mech, Electrodeposition of composite $Ni\text{-}TiO_2$ coatings from aqueous acetate baths, Metall. Mater. Trans. A 50 (2019) 4275–4287, https://doi.org/10.1007/s11661-019-05325-7.

[39] K. Mech, A novel magnetoelectrochemical method of synthesis of photoactive $Ni\text{-}TiO_2$ coatings from glycinate electrolytes, Mater. Des. 182 (2019) 108055, https://doi.org/10.1016/j.matdes.2019.108055.

[40] S. Ozden, L. Delafontaine, T. Asset, S. Guo, K.A. Filsinger, R.D. Priestley, P. Atanassov, C.B. Arnold, Graphene-based catalyst for CO_2 reduction: The critical role of solvents in materials design, J. Catal. 404 (2021) 512–517, https://doi.org/10.1016/j.jcat.2021.10.014.

[41] N. Rashid, M.A. Bhat, A. Das, P.P. Ingole, Unprecedented lower over-potential for CO_2 electro-reduction on copper oxide anchored to graphene oxide microstructures, J. CO_2 Util. 39 (2020) 101178, https://doi.org/10.1016/j.jcou.2020.101178.

[42] M.N. Hossain, J. Wen, A. Chen, Unique copper and reduced graphene oxide nanocomposite toward the efficient electrochemical reduction of carbon dioxide, Nature 7 (2017) 3184, https://doi.org/10.1038/s41598-017-03601-3.

[43] A.T. Smith, A.M. LaChance, S. Zeng, B. Liu, L. Sun, Synthesis, properties, and applications of graphene oxide/reduced graphene oxide and their nanocomposites, Nano Mater. Sci. 1 (2019) 31–47, https://doi.org/10.1016/j.nanoms.2019.02.004.

[44] N. Singh, P. Siwatch, J. Kaushal, J. Sharma, S.K. Tripathi, One-step green synthesis of reduced graphene oxide by electrochemical etching of carbon rods and effect of different bias voltages on the quality, J. Solid State Chem. 291 (2020) 121537, https://doi.org/10.1016/j.jssc.2020.121537.

[45] K.K.H. De Silva, H.-H. Huang, R. Joshi, M. Yoshimura, Restoration of the graphitic structure by defect repair during the thermal reduction of graphene oxide, Carbon 166 (2020) 74–90, https://doi.org/10.1016/j.carbon.2020.05.015.

[46] J. Shin, J.N. Heo, J.Y. Do, Y.-I. Kim, S.J. Yoon, Y.S. Kim, M. Kang, Effective charge separation in $rGO/NiWO_4$@Au photocatalyst for efficient CO_2 reduction under

visible light, J. Ind. Eng. Chem. 81 (2020) 427–439, https://doi.org/10.1016/j.jiec.2019.09.033.
[47] L. Tu, Y. Hou, G. Yuan, Z. Yu, S. Qin, Y. Yan, H. Zhu, H. Lin, Y. Chen, S. Wang, Bio-photoelectrochemcial system constructed with $BiVO_4$/RGO photocathode for 2,4-dichlorophenol degradation: $BiVO_4$/RGO optimization, degradation performance and mechanism, J. Hazard. Mater. 389 (2020) 121917, https://doi.org/10.1016/j.jhazmat.2019.121917.
[48] M.Z. Rahman, P. Maity, O.F. Mohammed, J. Gascon, Insight into the role of reduced graphene oxide in enhancing photocatalytic hydrogen evolution in disordered carbon nitride, Phys. Chem. Chem. Phys. 24 (2022) 11213–11221, https://doi.org/10.1039/D2CP00200K.
[49] S.A. Carminati, I. Rodríguez-Gutiérrez, A. de Morais, B.L. da Silva, M.A. Melo, F. L. Souza, A.F. Nogueira, Challenges and prospects about the graphene role in the design of photoelectrodes for sunlight-driven water splitting, RSC Adv. 11 (2021) 14374–14398, https://doi.org/10.1039/D0RA10176A.
[50] R. Suresh, R. Udayabhaskar, C. Sandoval, E. Ramírez, R.V. Mangalaraja, H. D. Mansilla, D. Contreras, J. Yáñez, Effect of reduced graphene oxide on the structural, optical, adsorption and photocatalytic properties of iron oxide nanoparticles, N. J. Chem. 42 (2018) 8485–8493, https://doi.org/10.1039/C8NJ00321A.
[51] L. Sang, L. Lei, C. Burda, Electrochemical fabrication of rGO-embedded Ag-TiO_2 nanoring/nanotube arrays for plasmonic solar water splitting, Nanomicro Lett. 11 (2019) 97, https://doi.org/10.1007/s40820-019-0329-2.
[52] J. Prakash, U. Prasad, R. Alexander, J. Bahadur, K. Dasgupta, A.N.M. Kannan, Photoelectrochemical solar water splitting: the role of the carbon nanomaterials in bismuth vanadate composite photoanodes toward efficient charge separation and transport, Langmuir 35 (2019) 14492–14504, https://doi.org/10.1021/acs.langmuir.9b02782.
[53] Z. Pan, G. Zhang, X. Wang, Polymeric carbon nitride/reduced graphene oxide/Fe_2O_3: all-solid-state Z-scheme system for photocatalytic overall water splitting, Angew. Chem. Int. Ed. Engl. 58 (2019) 7102–7106, https://doi.org/10.1002/anie.201902634.
[54] S.-H. Liu, J.-S. Lu, Y.-C. Pu, H.-C. Fan, Enhanced photoreduction of CO_2 into methanol by facet-dependent Cu_2O/reduce graphene oxide,, J. CO_2 Util. 33 (2019) 171–178, https://doi.org/10.1016/j.jcou.2019.05.020.
[55] X. An, K. Li, J. Tang, Cu_2O/reduced graphene oxide composites for the photocatalytic conversion of CO_2, ChemSusChem 7 (2014) 1086–1093, https://doi.org/10.1002/cssc.201301194.
[56] A. Wang, X. Li, Y. Zhao, W. Wu, J. Chen, H. Meng, Preparation and characterizations of Cu_2O/reduced graphene oxide nanocomposites with high photo-catalytic performances, Powder Technol 261 (2014) 42–48, https://doi.org/10.1016/j.powtec.2014.04.004.
[57] M. Bisetto, S. Rej, A. Naldoni, T. Montini, M. Bevilacqua, P. Fornasiero, CO_2 electroreduction by engineering the Cu_2O, RGO Inter 14 (2024) 412, https://doi.org/10.3390/catal14070412.
[58] C. Peng, B. Yao, L. Wang, X. Wan, Selectively electrolyzing CO_2 to ethylene by a Cu–Cu_2O/rGO catalyst derived from copper hydroxide nanostrands/graphene oxide nanosheets, RSC Adv. 14 (2024) 36602–36609, https://doi.org/10.1039/D4RA07259F.
[59] J. Hormes, W. Klysubun, J. Göttert, H. Lichtenberg, A. Maximenko, K. Morris, P. Nita, A. Prange, J. Szade, L. Wagner, M. Zając, A new SOLARIS beamline optimized for X-ray spectroscopy in the tender energy range, Nucl. Instrum. Methods Phys. Res. B: Beam Interact. Mater. At. 489 (2021) 76–81, https://doi.org/10.1016/j.nimb.2020.12.017.
[60] J. Szlachetko, J. Szade, E. Beyer, W. Błachucki, P. Ciochoń, P. Dumas, K. Freindl, G. Gazdowicz, S. Glatt, K. Guła, J. Hormes, P. Indyka, A. Klonecka, J. Kołodziej, T. Kołodziej, J. Korecki, P. Korecki, F. Kosiorowski, K. Kosowska, G. Kowalski, M. Kozak, P. Kozioł, W. Kwiatek, D. Liberda, H. Lichtenberg, E. Madej, A. Mandziak, A. Marendziak, K. Matlak, A. Maximenko, P. Nita, N. Olszowska, R. Panaś, E. Partyka-Jankowska, M. Piszak, A. Prange, M. Rawski, M. Roman, M. Rosmus, M. Sikora, J. Sławek, T. Sobol, K. Sowa, N. Spiridis, J. Stępień, M. Szczepanik, M. Ślęzak, T. Ślęzak, T. Tyliszczak, G. Ważny, J. Wiechecki, D. Wilgocka-Ślęzak, B. Wolanin, P. Wróbel, T. Wróbel, M. Zając, A. Wawrzyniak, M. Stankiewicz, SOLARIS National Synchrotron Radiation Centre in Krakow, Poland, 138 (2023) 10.
[61] B. Ravel, M. Newville, ATHENA, ARTEMIS, HEPHAESTUS: data analysis for X-ray absorption spectroscopy using IFEFFIT, J Synchrotron Radiat. 12 (2005) 537–541, https://doi.org/10.1107/S0909049505012719.
[62] K. Mech, M. Bisztyga-Szklarz, K. Szaciłowski, Brief insights into Cu_2O electrodeposition: detailed progressive voltammetric and electrogravimetric analysis of a copper lactate system, J. Electrochem. Soc. 167 (2020) 042504, https://doi.org/10.1149/1945-7111/ab7a83.
[63] Q.T. Du, J.S. Tan, Q.T. Wang, C.Y. Li, X.H. Liu, R.S. Cai, Y.H. Ding, Y.Q. Wang, Electrochemical deposition and formation mechanism of single-crystalline Cu_2O octahedra on aluminum, J. Anal. Methods Chem. 2012 (2012) 406162, https://doi.org/10.1155/2012/406162.
[64] S. Ali, A. Razzaq, H. Kim, S.-I. In, Activity, selectivity, and stability of earth-abundant CuO/Cu_2O/Cu^0-based photocatalysts toward CO_2 reduction, Chem. Eng. J. 429 (2022) 131579, https://doi.org/10.1016/j.cej.2021.131579.
[65] Z.H. Gan, G.Q. Yu, B.K. Tay, C.M. Tan, Z.W. Zhao, Y.Q. Fu, Preparation and characterization of copper oxide thin films deposited by filtered cathodic vacuum arc, J. Phys. D. Appl. Phys. 37 (2004) 81, https://doi.org/10.1088/0022-3727/37/1/013.
[66] X. Jiang, M. Zhang, S. Shi, G. He, X. Song, Z. Sun, Influence of applied potential on the band gap of Cu/Cu_2O thin films, J. Electrochem. Soc. 161 (2014) D640, https://doi.org/10.1149/2.0181412jes.
[67] M.B. Akbar, Y. Wang, X. Zhang, T. He, Study on photoelectrochemical CO_2 reduction over Cu_2O, J. Photochem. Photobiol. A 437 (2023) 114483, https://doi.org/10.1016/j.jphotochem.2022.114483.
[68] M. Zhao, Y. Jiang, J. Lv, Y. Sun, L. Cao, G. He, M. Zhang, Z. Sun, Microstructure, morphology and sunlight response of cuprous oxide thin films, J. Mater. Sci. - Mater. El. 27 (2016) 1799–1804, https://doi.org/10.1007/s10854-015-3956-5.
[69] N. Altaf, S. Liang, R. Iqbal, M. Hayat, T.R. Reina, Q. Wang, Cu-CuO_x/rGO catalyst derived from hybrid LDH/GO with enhanced C_2H_4 selectivity by CO_2 electrochemical reduction, J. CO_2 Util. 40 (2020) 101205, https://doi.org/10.1016/j.jcou.2020.101205.
[70] Q. Zhang, L. Huang, S. Kang, C. Yin, Z. Ma, L. Cui, Y. Wang, CuO/Cu_2O nanowire arrays grafted by reduced graphene oxide: synthesis, characterization, and application in photocatalytic reduction of CO_2, RSC Adv. 7 (2017) 43642–43647, https://doi.org/10.1039/C7RA07310K.
[71] Y. Wang, L. Cheng, W. Ge, Y. Zhu, J. Zhang, R. Chen, L. Zhang, Y. Li, C. Li, Effect of Charge on Carbon Support on the Catalytic Activity of Cu_2O toward CO_2 Reduction to C_2 Products, ACS Appl. Mater. Interfaces. 15 (2023) 23306–23315, https://doi.org/10.1021/acsami.3c03083.
[72] A. Sheelam, A. Muneeb, B. Talukdar, R. Ravindranath, S.-J. Huang, C.-H. Kuo, R. Sankar, Flexible and free-standing polyvinyl alcohol-reduced graphene oxide-Cu_2O/CuO thin films for electrochemical reduction of carbon dioxide, J. Appl. Electrochem. 50 (2020) 979–991, https://doi.org/10.1007/s10800-020-01450-z.
[73] Z. Zhang, X. Wang, H. Tian, H. Jiao, N. Tian, L. Bian, Y. Liu, Z.-L. Wang, Highly dispersed Cu-Cu_2O-CeO_x interfaces on reduced graphene oxide for CO_2 electroreduction to C_{2+} products, J. Colloid Interface Sci. 661 (2024) 966–976, https://doi.org/10.1016/j.jcis.2024.01.173.
[74] X. Wen, Z. Yang, L. Gao, R. Wei, X. Pan, J. Zhang, G. Xiao, Controllable dual Cu–Cu_2O sites derived from Cu_xAl-LDH for CO_2 electroreduction to hydrocarbons, Vac 222 (2024) 112974, https://doi.org/10.1016/j.vacuum.2024.112974.
[75] D.C.B. Alves, R. Silva, D. Voiry, T. Asefa, M. Chhowalla, Copper nanoparticles stabilized by reduced graphene oxide for CO_2 reduction reaction, Mater. Renew. Sustain. Energy 4 (2015) 2, https://doi.org/10.1007/s40243-015-0042-0.
[76] W.-Y. Zhi, Y.-T. Liu, S.-L. Shan, C.-J. Jiang, H. Wang, J.-X. Lu, Efficient electroreduction of CO_2 to C_2-C_3 products on Cu/Cu_2O@N-doped graphene,, J. CO_2 Util. 50 (2021) 101594, https://doi.org/10.1016/j.jcou.2021.101594.
[77] Y. Liu, H. Liu, C. Wang, Y. Wang, J. Lu, H. Wang, Reconstructed Cu/Cu_2O(I) catalyst for selective electroreduction of CO_2 to C_{2+} products, Electrochem. Commun. 150 (2023) 107474, https://doi.org/10.1016/j.elecom.2023.107474.
[78] W. Li, P. Hou, Z. Wang, P. Kang, Synergistic effect of N-doped layered double hydroxide derived NiZnAl oxides in CO_2 electroreduction, Sust. Energ. Fuels 3 (2019) 1455–1460, https://doi.org/10.1039/C9SE00056A.
[79] C. Xu, X. Zhang, M.-N. Zhu, L. Zhang, P.-F. Sui, R. Feng, Y. Zhang, J.-L. Luo, Accelerating photoelectric CO_2 conversion with a photothermal wavelength-dependent plasmonic local field, Appl. Catal. B: Environ. 298 (2021) 120533, https://doi.org/10.1016/j.apcatb.2021.120533.
[80] I.N. Sequeda, A.M. Meléndez, Understanding the role of copper vacancies in photoelectrochemical CO_2 reduction on cuprous oxide, J. Phys. Chem. Lett. 13 (2022) 3667–3673, https://doi.org/10.1021/acs.jpclett.2c00751.
[81] A. Visibile, R.B. Wang, A. Vertova, S. Rondinini, A. Minguzzi, E. Ahlberg, M. Busch, Influence of strain on the band gap of Cu_2O, Chem. Mater. 31 (2019) 4787–4792, https://doi.org/10.1021/acs.chemmater.9b01122.
[82] O.E. Kongstein, U. Bertocci, G.R. Stafford, In situ stress measurements during copper electrodeposition on (111)-textured Au, J. Electrochem. Soc. 152 (2005) C116, https://doi.org/10.1149/1.1854093.
[83] S.J. Hearne, J.A. Floro, Mechanisms inducing compressive stress during electrodeposition of Ni, J. Appl. Phys. 97 (2004) 014901, https://doi.org/10.1063/1.1819972.
[84] H. Sadek, M. Halfawy, S.G. Abdu, Stress During the Electrodeposition of Copper on Copper Substrate, J. Electrochem. Soc. 102 (1955) 226, https://doi.org/10.1149/1.2430034.
[85] B. Kumar, B.K. Kaushik, Y.S. Negi, Perspectives and challenges for organic thin film transistors: materials, devices, processes and applications, J. Mater. Sci.: Mater. Electron. 25 (2014) 1–30, https://doi.org/10.1007/s10854-013-1550-2.
[86] Y. Luo, L. Niu, Y. Wang, P. Wen, Y. Gong, C. Li, S. Xu, Regulating the work function of Cu_2O films via crystal facet engineering with enhanced charge transfer and SERS activity, Appl. Surf. Sci. 607 (2023) 155095, https://doi.org/10.1016/j.apsusc.2022.155095.
[87] G.H. Jun, S.H. Jin, B. Lee, B.H. Kim, W.-S. Chae, S.H. Hong, S. Jeon, Enhanced conduction and charge-selectivity by N-doped graphene flakes in the active layer of bulk-heterojunction organic solar cells, Energy Environ. Sci. 6 (2013) 3000–3006, https://doi.org/10.1039/C3EE40963E.
[88] H. Ning, X. Wang, W. Wang, Q. Mao, Z. Yang, Q. Zhao, Y. Song, M. Wu, Cubic Cu_2O on nitrogen-doped carbon shells for electrocatalytic CO_2 reduction to C_2H_4, Carbon 146 (2019) 218–223, https://doi.org/10.1016/j.carbon.2019.02.010.
[89] M.C. Biesinger, Advanced analysis of copper X-ray photoelectron spectra, Surf. Interface Anal. 49 (2017) 1325–1334, https://doi.org/10.1002/sia.6239.
[90] M.C. Biesinger, L.W.M. Lau, A.R. Gerson, R.S.C. Smart, Resolving surface chemical states in XPS analysis of first row transition metals, oxides and hydroxides: Sc, Ti, V, Cu and Zn, Appl. Surf. Sci. 257 (2010) 887–898, https://doi.org/10.1016/j.apsusc.2010.07.08.
[91] P.C. Healy, S. Myhra, A.M. Stewart, XPS Studies of Planar Four-Coordinate Copper (II) and Copper(III) Complexes, Jpn. J. Appl. Phys. 26 (1987) L1884–L1887, https://doi.org/10.1143/JJAP.26.L1884.
[92] N.S. McIntyre, M.G. Cook, X-ray photoelectron studies on some oxides and hydroxides of cobalt, nickel, and copper, Anal. Chem. 47 (1975) 2208–2213, https://doi.org/10.1021/ac60363a034.